www.MaterialsViews.com

Clean WS_2 and MoS_2 Nanoribbons Generated by Laser-Induced Unzipping of the Nanotubes

*Kuraganti Vasu, Sharma S. R. K. C. Yamijala, Alla Zak, Kothandam Gopalakrishnan, Swapan K. Pati, and C. N. R. Rao**

Irradiation of WS_2 and MoS_2 nanotubes dispersed in a medium of dimethylformamide (DMF) by an UV excimer pulsed krypton fluoride (KrF) laser yields WS_2 and MoS_2 nanoribbons as established by scanning electron microscopy (SEM), transmission electron microscopy (TEM), and atomic force microscopy (AFM). Nanoribbons were formed by longitudinal unzipping of the nanotubes after 200 laser pulses. High-resolution TEM (HRTEM) images show the presence of zig-zag edges in the WS_2 ribbons, responsible for room temperature ferromagnetism. Density functional theory (DFT) calculations on MoS_2 nanotubes have helped to unravel the mechanism of the unzipping process.

Graphene nanoribbons (GNRs) are known to possess useful magnetic and electronic properties. These 1D nanostructures have potential applications in optoelectronics and spintronic devices. GNRs have been prepared by unzipping of carbon nanotubes (CNTs) by chemical oxidation, a method that has been commonly used by many workers.[1–5] This method, however, gives rise to oxygen functionalities on the surface of GNRs. In order to avoid surface oxygen functionalities and produce pure GNRs, laser-induced unzipping of CNTs has been employed.[6] Plasma etching–induced unzipping is another successful method to synthesize NRs starting from NTs. By this method, both GNRs and boron nitride NRs have been prepared.[7,8]

In the last 2–3 years, there has been great interest in the properties of metal dichalcogenides (TMD) nanosheets. Thus, nanosheets of MoS_2 are emerging as materials with exciting possibilities. Nanoribbons of TMDs are the obvious candidates for study, since quantum confinement and edge states are expected to give rise to new electronic and magnetic properties. Nanoribbons of MoS_2 and WS_2 with zig-zag edges are expected to be ferromagnetic and metallic, whereas armchair nanoribbons would be nonmagnetic and semiconducting.[9–12] Recently, WS_2NRs have been synthesized by means of chemical unzipping of WS_2 nanotubes using lithium intercalation followed by exfoliation in organic solvents.[13] This procedure may not be applicable universally and has the limitation that diffusivity of solvent molecules controls the unzipping process. Furthermore, chemical manipulation may not altogether avoid surface functionalities. In order to produce clean TMD nanoribbons, we have carried out laser-induced unzipping of the WS_2 nanotubes dispersed in dimethylformamide medium. We have found laser irradiation unzips WS_2NTs as well as MoS_2NTs along the longitudinal axis, yielding WS_2NRs and MoS_2NRs after 200 laser pulses. Unlike other methods,[13–15] laser unzipping is a versatile method for the production of high-quality NRs with controllable width, edge states, and defects. Interestingly, WS_2NRs exhibit good ferromagnetic hysteresis unlike the nanotubes. In order to understand the mechanism of unzipping, we have carried out DFT calculations.

The effect of laser irradiation on change in WS_2NTs structure was studied as a function of number of laser pulses at constant laser energy. **Figure 1** shows SEM and TEM images of pristine WS_2NTs and of NRs obtained after 200 laser pulses. The nanotubes have a diameter in the range 30–50 nm and length in tens of micrometers (Figure 1a). The average width of the ribbon is around 100 nm and it becomes narrow after a 120° kink (Figure 1b). To investigate the unzipping evolution with laser irradiation, we have examined the response of NTs after 100 and 150 pulses. The resulting SEM image after 100 pulses, shown as an inset in Figure 1b reveals opening of the NT (indicated by arrow) along the longitudinal axis. The SEM image after 150 pulses shows both the opening stage and the ribbon (Figure S1a, Supporting Information). By comparing the SEM images after 100, 150, and 200 laser pulses, we find that a small opening is initiated during the initial stage of the irradiation which then progressively propagates along the longitudinal axis and fully unzips the tube with increasing laser pulses. More than 70% of the WS_2NTs transformed to NRs after 200 laser pulses. In Figure 1c,d, we show low-magnification TEM images of WS_2NTs and NRs. The pristine NT has the multiwalled structure with outer and inner diameters of ≈50 and ≈17 nm, respectively. The segments of NR are associated with

Dr. K. Vasu, S. S. R. K. C. Yamijala,
K. Gopalakrishnan, Prof. S. K. Pati, Prof. C. N. R. Rao
Chemistry and Physics of Materials Unit
Theoretical Science Unit and International Centre for Materials Science
Jawaharlal Nehru Centre for Advanced Scientific Research
Jakkur P.O.
Bangalore 560064, India
E-mail: cnrrao@jncasr.ac.in
Dr. A. Zak
Faculty of Science
Holon Institute of Technology
Holon 58102, Israel

DOI: 10.1002/smll.201500350

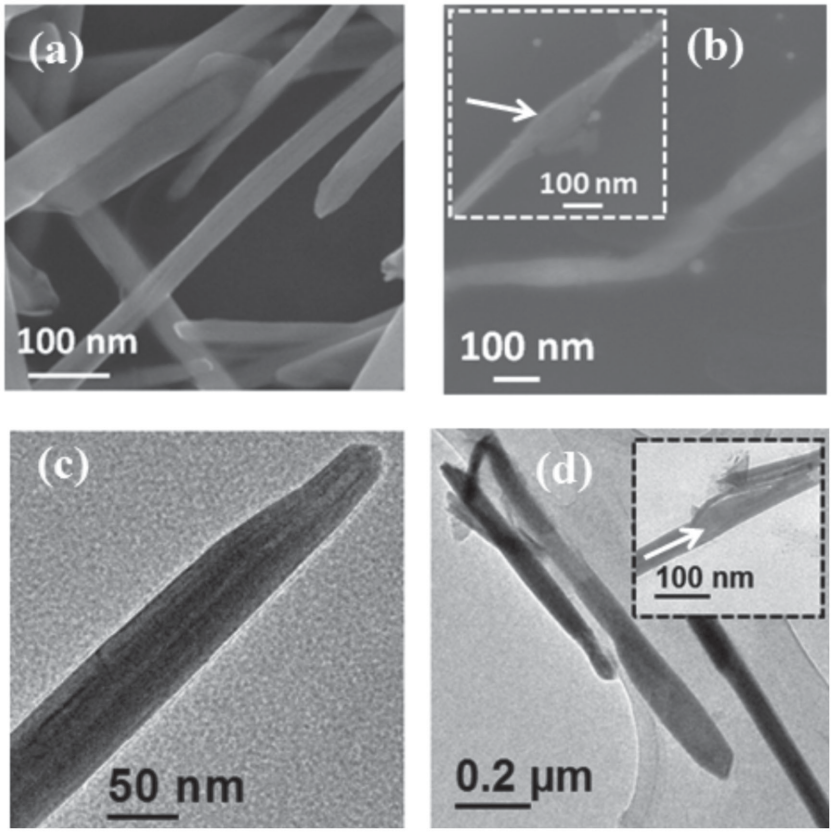

Figure 1. SEM and TEM images of pristine WS_2 a,c) nanotubes and b,d) nanoribbon. The opening of longitudinal axis of WS_2NT after 100 laser pulses is shown as inset of (b) and (d).

two kinks at 90° each (Figure 1d). The unzipping stage of NT after 100 laser pulses is shown as an inset of Figure 1d. The width of the NR is in the range 100–120 nm, however, the value changes in different segments. In addition to segments of the ribbon, the TEM image also contains long straight ribbons after 200 pulses (Figure S1b, Supporting Information). The NTs get destroyed when the laser energy and pulses exceed the optimal conditions mentioned earlier (Figure S1c, Supporting Information). From the SEM and TEM images, we observe that the WS_2NRs have a tendency toward mechanical bending and folding without any breakage.

Figure 2a,b shows typical AFM images with the corresponding height profiles of a WS_2NT and NR. From the AFM image, the height and diameter of the tube are found to be 10 and 60 nm, respectively, while the height and width of the ribbon is 3 and 150 nm, respectively. The height profile reveals the tube characterized by cylindrical geometry, whereas the ribbon surface has the expected flat geometry. From the various microscopic results presented above, we can conclude that laser-induced unzipping is a facile route to prepare good and flexible NRs of WS_2. The Raman spectrum of the WS_2NRs exhibits bands at 354.0 and 422.1 cm^{-1} due to the E^1_{2g} and A_{1g} modes. The corresponding bands in the case of NTs appear at 354.9 and 422.9 cm^{-1}, respectively. There is some softening of the E^1_{2g} and A_{1g} modes in WS_2NRs (Figure S2, Supporting Information). The intensity and full width at half maximum of both the modes in the NRs are higher than those of pristine NTs. This is attributed to quantum confinement and the changed electronic structure of NRs.[16] In Figure 2c, we show low-magnification TEM image of MoS_2 nanotubes with multiwalled structure containing 20–30 layers. The outer and inner diameters of the tube are 40 and 10 nm, respectively. The few-layer NRs obtained by laser irradiation (after 200 pulses) width around 90 nm can be seen from Figure 2d. The NR has a tendency to fold at the edges (indicated by arrow). SEM images of the MoS_2NTs and NRs are shown as insets of Figure 2c,d.

HRTEM images of WS_2NT and NR are presented in **Figure 3**a,b. The image in Figure 3a reveals that the NT is of high quality with the multiwalled structure without defects and stacking faults. The tube is composed of 20–25 layers with an interlayer separation 0.62 nm corresponding to (002) lattice plane WS_2. The outer and inner diameters of the tube are 30 and 10 nm, respectively. The electron diffraction (ED) pattern of WS_2NTs (Figure S3a, Supporting Information) displays superposition of diffraction spots that are elongated perpendicular to the tube axis, indicating the curvature of the multishell nanotube.[17] The few-layer nanoribbon has 5–6 layers (Figure 3b) with an interlayer separation similar to that in the NT. The ordered structure inside the ribbon arises from the Moire fringes caused by electron scattering from the ribbon slabs.[17] The ED pattern of WS_2NR is markedly different from that of the NT and the curvature-induced elongation of diffraction spots are absent. The hexagonal diffraction spots (Figure S3b, Supporting Information) in the ED pattern indicate flat geometry of WS_2NR with the molecular layers stacking along the *c*-axis parallel to the (001) plane. Different set of hexagonal spots is formed due to the mutual rotation of ribbon slabs with respect to one another owing to different stacking orders. The few-layer ribbon is characterized by many WS_2 nanosheets and these sheets get curved at the ribbon side edge (Figure S4a, Supporting Information). Because of this curvature, the width of nanoribbon is not exactly π times the diameter of the pristine nanotube. The atomic resolution edges of WS_2NR with the corresponding fast Fourier transformation (FFT) image are shown in Figure 3c. The image reveals that the ribbon has zig-zag edges with a defect (indicated by arrow). Under laser irradiation, the atoms can sputter out at the edges when the laser damage threshold exceeds the knock-on damage threshold of the WS_2 nanosheet. The zig-zag edges in the NRs are more likely to be located as kinks and foldable or bendable junctions.[18] The perfect hexagonal atomic structure formed by W and S atoms is found at the center of the single-layer NR without defects. The spacing between the protuberant dots in the line profile is 0.27 nm and corresponds to the (100) lattice plane of hexagonal WS_2 (Figure S4b, Supporting Information).

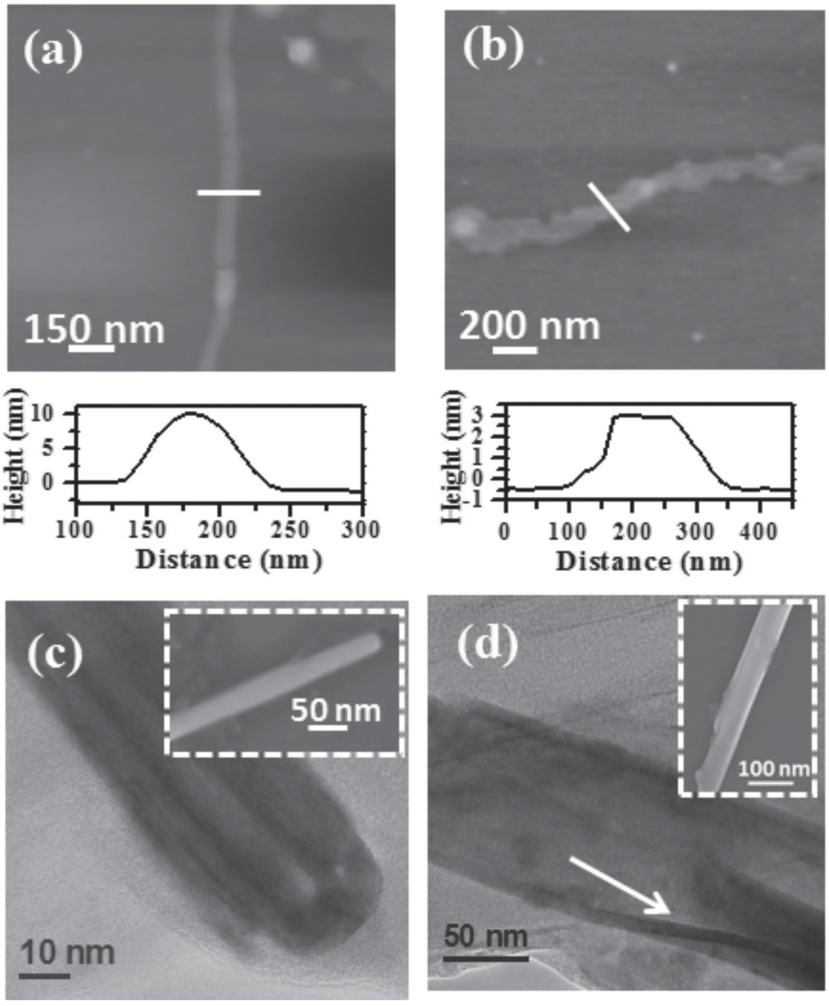

Figure 2. AFM images with corresponding height profiles of WS_2 a) nanotube and b) nanoribbon. Low-magnification TEM images of MoS_2 c) nanotube and d) nanoribbon with the corresponding SEM images as insets.

Density functional theory calculations on WS_2NRs show that zig-zag edges NRs are associated with ferromagnetism and metallic behavior.[11,12] The magnetism depends on the ribbon width, edge spins, and defects. The magnetization versus magnetic field (M–H) curves of WS_2NTs and NRs measured at 300 K in the field range –10 to +10 kOe are shown in Figure 3d. We observe a large difference in the hysteresis loops of the WS_2 NTs and NRs. After subtracting the diamagnetic contribution, the clear S-shaped curve with a saturation magnetization 0.01 emu g^{-1} is observed. The enlarged M–H curve in the field range –0.5 to +0.5 kOe (see inset) exhibits a remanent magnetization 0.0014 emu g^{-1} and a coercive field 100 Oe for WS_2NRs. Temperature-dependent magnetization curves measured at 100 Oe reveals the WS_2NRs have higher magnetic moments than NTs (Figure S5a, Supporting Information). Magnetization–temperature curves under field-cooled (FC) and zero field–cooled (ZFC) conditions show divergence (Figure S5b, Supporting Information) from quite high temperature (>400 K) unlike single-layer and few-layer WS_2 nanosheets.[19] Clearly, there is coexistence of antiferromagnetic and ferromagnetic interactions. Ferromagnetic characterization arises from edge states and defects. The edges would be present to a greater extent in nanoribbons. The divergence between FC and ZFC data in the temperature range 2–400 K indicate that the Curie temperature of the WS_2NRs is well above 400 K.[20]

DFT calculations have been carried out to understand the laser-induced unzipping mechanism of MoS_2 nanotubes. Since our experimental results show unzipping along the tube axis and zig-zag edged nanoribbons, DFT calculations were performed on armchair MoS_2NT of chirality (6, 6) consisting of 36 atoms in the unit cell. We have studied the energetics of the formation of various kinds of vacancies in the nanotubes as strong laser irradiation ruptures the nanotube. The structure of pristine MoS_2NT shown in **Figure 4**a has been generated by considering a supercell consisting of 252 atoms. Five types of possible vacancies were examined, namely, (i) a single Mo-vacancy; (ii) a triple Mo-vacancy with (a) all vacancies along the longitudinal axis (tube axis), (b) two along the longitudinal axis and one along lateral axis, (c) all vacancies along the lateral axis; and (iii) two S-vacancies. In **Table 1**, we present the energetics of defect stability, formation energy, and the defect formation with respect to 1-Mo vacancy.

From the energetic studies, we see that the formation energy of a Mo-vacancy is almost equal to the formation energy of a S-vacancy in armchair MoS_2NT, unlike in the case of MoS_2 nanosheets.[21,22] We find that creation of further Mo-vacancies is energetically feasible if they are created along the longitudinal axis than along the diameter of the tube. We also find an already created vacancy decreases (increases) the amount of energy required to create the next vacancy if the new vacancy is along the longitudinal axis (lateral axis). Figure 4b,c shows the optimized structures of MoS_2NT after creation of 2-S and 3-Mo longitudinal vacancies, respectively. Creation of a 2-S vacancy does not change the tube structure significantly except the formation of new bonds between Mo atoms (see circle in Figure 4b). However, creation of 3-Mo longitudinal vacancies changes the tube structure drastically and initiates the unzipping process along the tube axis. The unzipping process is not initiated by creating other combinations of 3-Mo vacancies (Figure S6, Supporting Information).

In order to understand the role of defects in the unzipping process, we have computed the density of states for MoS_2NT with 2-S and 3-Mo longitudinal vacancies and the results are shown in Figure 4d–f. The pristine (6, 6) MoS_2NT is a semiconductor with ≈0.2 eV bandgap and a NT with 2-S vacancies has a bandgap of ≈0.1 eV. A MoS_2NT with 3-Mo

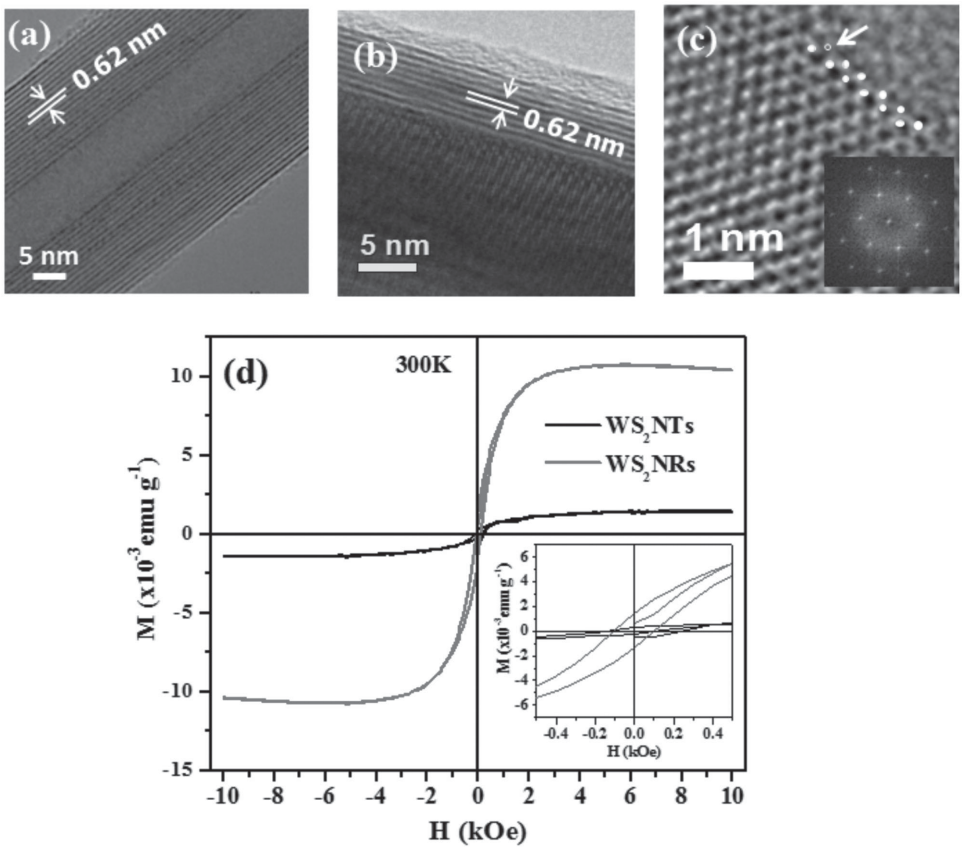

Figure 3. HRTEM images of a) pristine WS_2NT and b) few-layer WS_2NR. c) Zig-zag edges in a WS_2 nanoribbon with the corresponding fast Fourier transformation (FFT) image. d) Magnetization versus magnetic field (*M*–*H*) curves of WS_2 nanotubes and nanoribbons measured at room temperature. Inset shows enlarged part of the *M*–*H* curve of the nanoribbons.

vacancies clearly closes the gap and becomes metallic. The metallic nature would be associated with aligned magnetic moments. Furthermore, nanotubes with Mo-vacancies have both their conduction and valence band edges localized near the defects. As an external electric field, as with a laser (which goes in the Hamiltonian as $-nEr$, where n, E, and r are electron density, electric field strength, and atomic position respectively), interacts strongly with the atoms which have more charges, atoms near the defect sites become more vulnerable for further rupture and initiate unzipping.

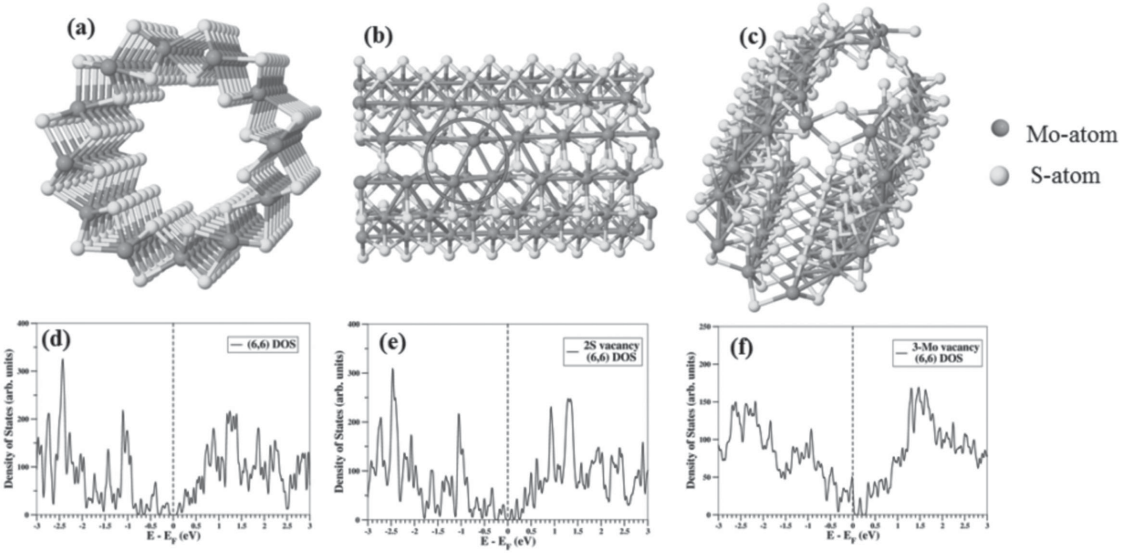

Figure 4. Structure of (6, 6) MoS_2 a) pristine nanotube b) after creation of 2-S vacancies and c) after creation of 3-Mo longitudinal vacancies. Variation of density of states of d) pristine MoS_2 nanotubes e) after creation of 2-S vacancies and f) after creation of 3-Mo longitudinal vacancies.

www.MaterialsViews.com

Table 1. Energetics of formation of different kinds of vacancies in MoS_2 nanotubes.

Vacancy type	$E_{defect} - E_{pristine}$ [eV]	$E_{Form} = E_{defect} - E_{pristine} - n \times E_{Mo/S}$ (±0.01 eV) [eV]	With respect to 1-Mo vacancy [eV]
1-Mo	221.922	2.806	0.000
3-Mo longitudinal	650.793	–6.554	–14.973
3-Mo longitudinal and lateral	664.184	6.837	–1.582
3-Mo lateral	667.268	9.921	1.502
2-S	559.104947	5.016	–
	(279.552/S)	(2.508/S)	

The solvent DMF also plays a role in the unzipping of MoS_2NTs. Since DMF molecules are dipolar, the positive side of their dipoles would be pointing at the defect sites. In the presence of a high external electric field, the defect (and solvent molecules) induced dipoles in the nanotube would align along the direction of the electric field to gain stability. Creation of Mo-vacancies along the longitudinal direction promotes induced dipoles to point along the same direction and hence minimizes their potential energy (which is not favorable in the lateral direction). Thus, longitudinal unzipping is more favorable than lateral unzipping for an armchair nanotube and the unzipping occurs through the creation of Mo-vacancies.

In conclusion, the present study demonstrates that laser irradiation is a convenient route to generate nanoribbons of WS_2 and MoS_2. Raman spectra of the ribbons show shifts in the bands relative to those in the nanotubes. The presence of zig-zag edges in the nanoribbons is clearly revealed by high-resolution TEM images. Accordingly, the nanoribbons show ferromagnetic hysteresis loops with saturation. DFT calculations have thrown light on the mechanism of unzipping of tubes and points to the role of defects and the occurrence longitudinal unzipping.

Supporting Information

Supporting Information is available from the Wiley Online Library or from the author.

Acknowledgements

K.V. thanks the DST-Postdoctoral fellowship in nanoscience and nanotechnology program for financial support. S.S.R.K.C.Y. and S.K.P. acknowledge TUE-CMS, JNCASR, for computational facilities and DST for funding.

[1] D. V. Kosynkin, A. L. Higginbotham, A. Sinitskii, J. R. Lomeda, A. Dimiev, B. K. Price, J. M. Tour, *Nature* **2009**, *458*, 872.
[2] Ch. Tao, L. Jiao, O. V. Yazyev, Y. Ch. Chen, J. Feng, X. Zhang, R. B. Capaz, J. M. Tour, A. Zettl, S. G. Louie, H. Dai, M. F. Crommie, *Nat. Phys.* **2011**, *7*, 616.
[3] L. Y. Jiao, X. R. Wang, G. Diankov, H. L. Wang, H. J. Dai, *Nat. Nanotechnol.* **2010**, *5*, 321.
[4] S. S. Rao, S. N. Jammalamadaka, A. Stesmans, V. V. Moshchalkov, J. van Tol, D. V. Kosynkin, A. Higginbotham-Duque, J. M. Tour, *Nano Lett.* **2012**, *12*, 121.
[5] S. S. Rao, A. Stesmans, D. V. Kosynkin, A. Higginbotham, J. M. Tour, *New J. Phys.* **2011**, *13*, 113004.
[6] P. Kumar, L. S. Panchakarla, C. N. R. Rao, *Nanoscale* **2011**, *3*, 2127.
[7] L. Jiao, L. Zhang, X. Wang, G. Diankov, H. Dai, *Nature* **2009**, *458*, 877.
[8] H. Zeng, Ch. Zhi, Z. Zhang, X. Wei, X. Wang, W. Guo, Y. Bando, D. Golberg, *Nano Lett.* **2010**, *10*, 5049.
[9] Y. Li, Z. Zhou, S. Zhang, Z. Chen, *J. Am. Chem. Soc.* **2008**, *130*, 16739.
[10] H. Pan, Y. W. Zhang, *J. Mater. Chem.* **2012**, *22*, 7280.
[11] F. L. Urias, A. L. Elias, N. P. Lopez, H. R. Gutierrez, M. Terrones, H. Terrones, *2D Mater.* **2015**, *2*, 015002.
[12] H. Zhang, X. B. Li, L. M. Liu, *J. Appl. Phys.* **2013**, *114*, 093710.
[13] C. Nethravath, A. A. Jeffery, M. Rajamathi, N. Kawamoto, R. Tenne, D. Golberg, Y. Bando, *ACS Nano* **2013**, *7*, 7311.
[14] D. G. Kvashnin, L. Y. Antipina, P. B. Sorokin, R. Tenne, D. Golberg, *Nanoscale* **2014**, *6*, 8400.
[15] J. Lin, Z. Peng, G. Wang, D. Zakhidov, E. Larios, M. J. Yacaman, J. M. Tour, *Adv. Energy Mater.* **2014**, *4*, 1301875.
[16] H. S. S. R. Matte, A. Gomathi, A. K. Manna, D. J. Late, R. Datta, S. K. Pati, C. N. R. Rao, *Angew. Chem.* **2010**, *122*, 4153.
[17] M. Remskar, Z. Skraba, M. Regula, Ch. Ballif, R. Sanjines, F. Levy, *Adv. Mater.* **1998**, *10*, 246.
[18] X. Li, X. Wang, L. Zhang, S. Lee, H. Dai, *Science* **2008**, *319*, 1229.
[19] C. N. R. Rao, H. S. S. R. Matte, K. S. Subrahmanyam, U. Maitra, *Chem. Sci.* **2012**, *3*, 45.
[20] Z. Yang, D. Gao, J. Zhang, Q. Xu, S. Shi, K. Tao, D. Xue, *Nanoscale* **2015**, *7*, 650.
[21] K. C. Santosh, R. C. Longo, R. Addou, R. M. Wallace, K. Cho, *Nanotechnology* **2014**, *25*, 375703.
[22] H. P. Komsa, A. V. Krasheninnikov, *Phys. Rev. B* **2015**, *91*, 125305.

Received: February 4, 2015
Revised: April 4, 2015
Published online: May 21, 2015